

1 **Subduction of trench-fill sediments beneath an**
2 **accretionary wedge: insights from sandbox analogue**
3 **experiments**

4 **Atsushi Noda¹, Hiroaki Koge^{2*}, Yasuhiro Yamada³, Ayumu Miyakawa¹,**
5 **Juichiro Ashi²**

6 ¹Geological Survey of Japan, National Institute of Advanced Industrial Science and Technology
7 (AIST), Central 7, Higashi 1-1-1, Tsukuba, Ibaraki 305-8567, Japan

8 ²Atmosphere and Ocean Research Institute, The University of Tokyo, 5-1-5 Kashiwanoha,
9 Kashiwa-shi, Chiba 277-8564, Japan

10 ³Japan Agency for Marine-Earth Science and Technology (JAMSTEC), 3173-25 Showa-machi,
11 Kanazawa, Yokohama 236-0001, Japan

12 **Key Points:**

- 13 • Progressive thickening of the accretionary wedge leads the décollement to step down
14 and narrows the subduction channel.
- 15 • Subduction of a rigid topographic high warps the décollement, thrusting trench-
16 fill sediment beneath the wedge.
- 17 • Widening of the subduction channel due to subduction of a topographic high en-
18 ables sediment to be subducted to a high-pressure environment.

*Present address, Geological Survey of Japan, National Institute of Advanced Industrial Science and
Technology (AIST)

Corresponding author: Atsushi Noda, a.noda@aist.go.jp

Abstract

Ancient exhumed accretionary complexes are sometimes associated with high-pressure–low-temperature (HP–LT) metamorphic rocks, such as psammitic schists, which are derived from sandy trench-fill sediment. At accretionary margins, sandy trench-fill sediments are rarely subducted to the depth of HP metamorphism because they are commonly scraped off at the frontal wedge. This study uses sandbox analogue experiments to investigate the role of seafloor topography in the transport of trench-fill sediment to depth during subduction. The experiments were conducted with a detached, rigid backstop to allow a topographic high (representing a seamount) to be subducted through a subduction channel. In experiments without topographic relief, progressive thickening of the accretionary wedge pushed the backstop down, leading to a stepping down of the décollement, narrowing the subduction channel, and underplating the wedge with subducting sediment. In contrast, in experiments with a topographic high, the subduction of the topographic high raised the backstop, leading to a stepping up of the décollement and widening of the subduction channel. These results suggest that the subduction of topographic relief is a possible mechanism for the transport of trench-fill sediment from the trench to HP environments through a subduction channel. A sufficient supply of sediment to the trench and topographic relief on the subducting oceanic plate might enable trench-fill sediment to be accreted at various depths and deeply subducted to become the protoliths of HP–LT metamorphic rocks.

Plain Language Summary

Ancient accretionary rocks are sometimes exposed close to high-pressure metamorphic rocks of the same depositional age, which were originally deposited at the trench and deformed at depth (>20 km) along the subduction zone. Because most trench-fill sandy sediment along accretionary margins is scraped off at the toe of the accretionary wedge, it is difficult to explain how sandy metamorphic rocks can coexist with accretionary rocks of the same depositional age. This study examines the importance of the surface roughness of the subducting oceanic crust in transporting sandy trench-fill sediment to high-pressure environments. We performed two types of sandbox analogue experiment, one with a smooth and one with a rough subducting plate surface. For the case of a smooth plate, the growing accretionary wedge pushed the sliding surface down, thereby preventing the sandy sediment from being subducted to depth and resulting in the stacking of

51 sediment trapped under the accretionary wedge (i.e., underplating). In contrast, a to-
52 pographic high on the subducting oceanic crust raised the sliding surface to accommo-
53 date both the topographic high and the surrounding sediment, meaning that the sed-
54 iment could then be subducted (i.e., underthrusting). This might explain the transport
55 of sandy sediment to the depths of high-pressure metamorphism.

56 **1 Introduction**

57 High-pressure–low-temperature (HP–LT) metamorphic rocks derived from terrige-
58 nous sedimentary rocks are known to occur at subduction margins. Such metamorphic
59 rocks are exposed alongside low-grade accretionary rocks and fore-arc basin strata that
60 include coarse-grained sandy deposits with the same depositional ages as the metamor-
61 phic rocks. For example, the Sanbagawa Metamorphic Complex in southwestern Japan
62 contains HP–LT psammitic and even conglomeratic schists (e.g., Wallis, 1998), and the
63 depositional ages and geochemical characteristics of the protolith are almost identical
64 to those of sandstone from the low-grade Shimanto Accretionary Complex (Kiminami
65 et al., 1999; Shibata et al., 2008; Aoki et al., 2012) and submarine fan turbidites deposited
66 in the associated fore-arc basin (Noda & Sato, 2018) (Figure 1). These observations in-
67 dicate that terrigenous trench-fill sediments were accreted in a shallow subduction zone
68 and were also subducted to >20 km depth. Other examples of such subduction–accretion-
69 related HP–LT metamorphic rocks can be seen in the Franciscan Complex in Califor-
70 nia (e.g., Ernst, 2011; Jacobson et al., 2011; Dumitru et al., 2015; Raymond, 2018), the
71 Chugach terrane in Alaska (Plafker et al., 1994), the Central Pontides in Turkey (Okay
72 et al., 2006), and the Coastal Cordillera in Chile (Glodny et al., 2005; Willner et al., 2004;
73 Angiboust et al., 2018).

74 At typical sedimentary accretion zones, such as those in Cascadia (Gulick et al.,
75 1998; Booth-Rea et al., 2008; Calvert et al., 2011), Alaska (J. C. Moore et al., 1991; Ye
76 et al., 1997), Java (Kopp et al., 2009), southern Chile (Glodny et al., 2005; Melnick et
77 al., 2006), Sumatra (Singh et al., 2008; Huot & Singh, 2018), and Japan (Park et al., 2002;
78 H. Kimura et al., 2010), terrigenous trench-fill sediments are generally scraped off at the
79 frontal wedge, whereas hemipelagic-to-pelagic sediments underplate the base of the ac-
80 cretionary wedge (e.g., Scholl, 2019). This may be because the increased structural thick-
81 ness of the wedge and progressive dewatering of subducting sediment causes the décollement
82 to step down and narrow the subduction channel (e.g., Sample & Moore, 1987; Vannuc-

83 chi et al., 2008). This suggests that the growth of the accretionary wedge might inhibit
84 the subduction of terrigenous sediment beyond the wedge through the subduction chan-
85 nel. However, occurrences of HP–LT metasediment at some accretionary margins demon-
86 strate that terrigenous sediment can be subducted beneath the wedge. One hypothesis
87 is that a topographic high enables trench-fill sediment to be subducted under the wedge
88 (Figure 2). Subducting seamounts followed by subducting material can be observed be-
89 neath the wedge along accretionary margins in southwestern Japan (G. F. Moore et al.,
90 2014), Alaska (Li et al., 2018), Barbados (G. F. Moore et al., 1995), and Hikurangi (Barker
91 et al., 2009; Bell et al., 2010).

92 The subduction of terrigenous material associated with the rough topography of
93 a subducting oceanic plate has been proposed to explain tectonic erosion of the wedge
94 (e.g., von Huene & Culotta, 1989; Lallemand et al., 1994; von Huene et al., 2004). Sand-
95 box analogue experiments have shown the potential for sediment transport below the frontal
96 wedge behind a subducting topographic high (Lallemand et al., 1992; Dominguez et al.,
97 2000). Numerical simulations show that in the wake of a subducting seamount, there are
98 unfaulted strata, large-offset thrust faults, increased fault spacing, an oversteepened sur-
99 face slope, and intense deformation along the base of the wedge (Morgan & Bangs, 2017).
100 In addition, recent seismic profiles across the accretionary margins of the Nankai Trough
101 (Bangs et al., 2006) and the Hikurangi Trench (Bell et al., 2010) reveal that subduct-
102 ing seamounts or ridges and the surrounding sediment are accommodated by a step-up
103 in the décollement, and the surrounding sediment is being transported to depth.

104 However, the influence of a subducting seamount beneath an accretionary wedge
105 on subduction and accretion fluxes is not well understood. In particular, the role of to-
106 pographic highs in modifying the décollement level and in maintaining or rejuvenating
107 the subduction channel as a conduit for sediment subduction needs to be explored. The
108 purpose of this study is (1) to investigate how the topographic roughness of the subduct-
109 ing plate interface influences material fluxes, including the accretion of sediment to the
110 wedge and the subduction of sediment along the subduction channel, and (2) to propose
111 a model that explains how terrigenous trench-fill sediment can be transported to depth.
112 We performed two types of sandbox analogue experiment, one with and one without a
113 topographic high. The novelty of these experiments is that they used a detached back-
114 stop to reproduce the subduction and underplating of sediment when a rigid topographic
115 high is subducted beneath an accretionary wedge. We also inserted two weak layers within

116 the sand, to reproduce the situation where the subducting sediment includes several po-
117 tential slip surfaces. Such multiple décollements are commonly found within underthrust
118 sediments or at the top of the oceanic crust, including at the Nankai (G. F. Moore et
119 al., 2001; Park et al., 2002), Hikurangi (Ghisetti et al., 2016; Plaza-Faverola et al., 2016),
120 and Barbados (Saffer, 2003) accretion zones.

121 **2 Methods**

122 **2.1 Model setup and experimental materials**

123 A scaled 2-D analogue modeling technique was used for this study so that the re-
124 sults could be compared with naturally occurring geological structures (e.g., Buiter, 2012;
125 Graveleau et al., 2012). A glass-sided rectangular deformation rig with internal dimen-
126 sions of 100 cm \times 30 cm \times 20 cm was used (Figure 3). A steel plate was positioned at
127 one end as a fixed wall with a small open window at the bottom. A rigid wedge made
128 from wood was placed next to the steel plate but was not fixed to it. The wedge was de-
129 signed to behave like a static backstop that has a higher mechanical strength than the
130 accretionary wedge (e.g., Tsuji et al., 2015). A rigid backstop is used to ensure stabil-
131 ity during the experiments and for repeatability. The mobility of the backstop helped
132 to replicate the deformable nature of equivalent structures in natural geological systems,
133 and to allow topographic relief to be subducted. The backstop had a surface slope that
134 dips at 30° and is covered by sandpaper. A plastic (Mylar®) sheet was placed over the
135 rig’s base plate and fixed to a roll that pulled the sheet using a stepper motor (on the
136 left side in Figure 3). The sheet was pulled beneath the rigid backstop at a rate of 0.5 cm/min,
137 thereby compressing the experimental material above.

138 Two types of granular material were used for the experiments: Toyoura sand and
139 glass micro-beads. Dry granular materials like these are widely used as analogue mate-
140 rials to simulate the brittle and frictional behavior of sedimentary rocks in accretionary
141 wedges because they display elastic–frictional plastic behavior and reproduce the non-
142 linear deformation of crustal rocks under brittle conditions (e.g., Dahlen, 1984; Lohrmann
143 et al., 2003; Graveleau et al., 2012). Toyoura sand, a standard testing material commonly
144 used by Japanese civil engineers, is a spherical quartz-rich sand with a particle size of
145 0.14–0.26 mm ($D_{50} = 0.2$ mm), a density of approximately 1600 kg m⁻³, an internal co-
146 efficient of friction, μ , of 0.59–0.68, and a cohesion, C , of 105–127 Pa (Yamada et al., 2006;

147 Dotare et al., 2016). The glass micro-beads are spherical and 0.045–0.063 mm in diam-
148 eter, have a low internal coefficient of friction ($\mu = 0.47$) and low cohesion (40 Pa), and
149 are considered a suitable analogue for weaker layers (Yamada et al., 2006, 2014).

150 Layers of sand and glass micro-beads with a total thickness of 3.4 cm were used
151 in the experiments. The sand and glass were sprinkled into the rig from a height of ap-
152 proximately 30 cm above the rig floor (Figure 3). Alternating layers of blue, red, and
153 black sand were laid down to help visualize the cross-sectional geometry of the models,
154 without influencing the mechanical homogeneity. Mechanically weak layers were created
155 by adding two thin layers of glass micro-beads, each 3 mm thick.

156 Experiment A (Exp. A) investigated the subduction of a smooth oceanic plate be-
157 neath a static backstop (Figure 3a). Experiment B (Exp. B) investigated the subduc-
158 tion of topographic relief (e.g., a seamount), using a block that was attached to the plas-
159 tic sheet (Figure 3b). The height of the relief was 1.6 cm, approximately half of the to-
160 tal thickness of the sediment. The height of the relief was chosen to avoid drastic defor-
161 mation of the accretionary wedge. The surface of the topographic relief was covered by
162 a Teflon[®] sheet. The total amount of horizontal shortening was 30 cm for Exp. A and
163 35 cm for Exp. B.

164 After each 2 cm increment of shortening, we sprinkled dry sand from at least 10 cm
165 above the surface of the accretionary wedge to fill the topographic lows that had devel-
166 oped (Figure 4). This sand was used to replicate sedimentation in fore-arc/slope basins
167 that form on the surfaces of accretionary wedges. A total of 1129 g of sand was added
168 over the course of Exp. A and 910 g during Exp. B. The volumes of sand added during
169 Exp. A and B were 706 and 569 cm³, respectively.

170 In addition to investigating wedge morphology, we studied temporal variations in
171 sediment influx/outflux. The sediment influx and outflux (cm²) were calculated using
172 the thicknesses (cm) of the trench-fill sediments (influx) and the subduction channel un-
173 derneath the backstop (outflux), which were multiplied by the rig width (30 cm) and di-
174 vided by the length of shortening (cm). Input and output (cm³) are here defined to be
175 the integrals of influx and outflux, respectively, with respect to shortening length (cm).
176 Time-lapse digital images were taken through the transparent side glass at 5 s intervals
177 using a PC-based controller. The images were later analyzed to calculate sediment in-
178 flux/outflux and to study the cross-sectional geometry of the wedges. The experiments

179 did not account for the effects of isostatic compensation and erosion, which would have
 180 contributed to the differences between our models and natural examples (e.g., Schellart
 181 & Strak, 2016).

182 **2.2 Scaling**

183 Models used in laboratory experiments should be properly scaled so that the re-
 184 sults can be considered true analogues of geological processes (e.g., Hubbert, 1937). It
 185 is assumed that brittle deformation will obey frictional Mohr–Coulomb-type laws. The
 186 basic scaling relationship between the physical properties of a model and those in na-
 187 ture, which relates the stress, σ , density, ρ , gravity, g , and length, l (Hubbert, 1937; Schel-
 188 lart, 2000) is

$$\frac{\sigma_g}{\sigma_m} = \frac{l_g}{l_m} \times \frac{g_g}{g_m} \times \frac{\rho_g}{\rho_m}. \quad (1)$$

189 where the subscripts m and g indicate model and geological values, respectively. The co-
 190hesion C can substitute for stress, σ (Schellart, 2000; Graveleau et al., 2012), and the
 191experiments are performed under normal gravity ($g_m/g_g = 1$); consequently, Eq. 1 can
 192be modified to give

$$\frac{l_g}{l_m} = \frac{C_g}{C_m} \times \frac{\rho_m}{\rho_g}. \quad (2)$$

193 For mean bulk density values of 2000–2500 kg m⁻³ and cohesion values of 5–20 MPa,
 194 which are typical of sedimentary rocks in accretionary wedges (Schumann et al., 2014),
 195 the length scale ratio ranges from approximately 3×10^4 to 1×10^5 . A 1 cm model layer
 196 in an experiment therefore corresponds to 300 m to 1 km in nature. The 3.4-cm-thick
 197 sediment layers used in this experiment can be scaled to 1–3 km of strata, which is a mod-
 198erate thickness of trench-fill sediment for a modern accretionary margin (Noda, 2016).
 199 The 5 cm width and 1.6 cm height of the topographic relief used in Exp. B can be scaled
 200 to 1.5–5 km and 0.5–1.6 km, respectively. The scaled dimensions of the topographic re-
 201 lief are comparable to many seamounts on the Pacific plate. However, the height-to-radius
 202 ratio of 0.64 in the model is higher than that of 0.21 for natural seamounts (Jordan et
 203 al., 1983; Smith, 1988). This high ratio is used to enhance the effects of topography. The
 204 total amount of shortening during the experiments was 30–35 cm, which is equivalent

205 to 9–35 km of displacement. Assuming a plate convergence rate of 5 cm/year, this in turn
206 corresponds to $1.8\text{--}7 \times 10^5$ years. A sediment supply to the topographic lows of 910–1129 g
207 for 6×10^5 years is equivalent to a sediment budget on the order of 10^6 t/year. The cal-
208 culated sediment budget is the same order of magnitude as the sediment load in many
209 mountainous rivers in Japan and New Zealand (Milliman & Syvitski, 1992), and the sed-
210 imentary influx into the Kumano Basin during the last 4 Myr ($50 \text{ km} \times 70 \text{ km} \times 2 \text{ km}$).

211 **3 Results**

212 **3.1 Experiment A: Subduction without a seamount**

213 During the first ~ 9 cm of shortening, high-frequency, low-amplitude forethrusts de-
214 veloped in front of the backstop (Stage 1, Figure 5a; 8 cm of shortening in Figure 6). The
215 wedge was uplifted quickly (uplift rate is 0.34 in Figure 5d), and thus the slope increased
216 rapidly, exceeding 12° by the end of Stage 1 (Figure 5c). After the emergence of T_6 (Stage
217 2), the frequency of forethrust initiation and the uplift rate of the wedge (0.10) were lower
218 than during Stage 1, but the rate of wedge widening (0.22) remained nearly constant (Fig-
219 ure 5). The slope of the wedge surface ranged from 8.5° to 13° , and was 9.5° at the end
220 of the experiment (Figure 5c).

221 Deformation was concentrated in the upper layer of glass beads, which acted as a
222 décollement, until 16 cm of shortening (Figure 6). At around 18 cm of shortening the
223 décollement stepped down to the lower layer of glass beads as the toe of the backstop
224 subsided below the upper layer of glass beads. During this stage, the footwall of fore-
225 thrust T_7 underthrust the wedge and the sand layer between the two layers of glass beads
226 underplated the wedge, creating a duplex structure (18–24 cm of shortening in Figure 6).
227 This underthrusting raised the hanging wall of T_7 and created a piggy-back basin (trench-
228 slope basin) on top of the wedge (22 cm of shortening). After the activation of T_8 , with
229 the lower layer of glass beads acting as a décollement, subducting sediment was accreted
230 to both the frontal and basal parts of the wedge with increasing amount of underplat-
231 ing and thickness of the forethrust sheet of T_8 . The final forethrust, T_9 , was initiated
232 with the upper layer of glass beads acting as the detachment (30 cm of shortening). The
233 final wedge was nearly 30 cm in length and had a constant slope of 9.5° (Figure 5). The
234 toe of the backstop further subsided, to the lower layer of glass beads (30 cm of short-
235 ening in Figure 6).

236 The outflux from the subduction channel (sediment subduction) gradually decreased,
 237 but its rate of change increased (Figure 5e). In particular, after the décollement stepped
 238 down, the outflux dropped rapidly. Influx to the accretionary wedge (solid dashed line
 239 in Figure 5e) increased to balance the total sediment influx. The output-to-input ratio
 240 of the experiment was 0.36 (Table 1).

241 **3.2 Experiment B: Subduction with a seamount**

242 Stage 1 of Exp. B was almost identical to that of Exp. A in terms of wedge progra-
 243 dation, and the widening and uplift rates of the wedge (Figure 5a–d). Stage 2 started
 244 after the initiation of forethrust T_5 , earlier than in Exp. A. T_5 was active for over 12.8 cm
 245 of shortening, exceeding that of any other forethrust in either experiment (Figure 5a).
 246 This long activity acted to reduce the width of the wedge and steepened its slope to 17.7°
 247 (Figure 5b, c). The wedge progradation rate during Stage 2 was 0.10, nearly half that
 248 of Exp. A (Figure 5a). The uplift rate varied from 0.06 to 0.29, but the mean rate was
 249 the same as in Exp. A (Figure 5b).

250 The wedge deformation process during Stage 1 of Exp. B was similar that in Exp. A
 251 (0–6 cm of shortening in Figure 7). However, at 7 cm of shortening, the seamount trig-
 252 gered the first forethrust of Stage 2 at 10 cm from the toe of the wedge (T_5 in Figure 7).
 253 The subduction of the seamount led to an undeformed layer underthrusting the wedge,
 254 and then uplifted the hanging wall as a trench-slope basin to create accommodation space
 255 (10–16 cm of shortening in Figure 7).

256 A décollement was formed in the upper layer of glass beads on the landward side
 257 of the seamount and in T_5 on the trenchward side during the period between the initi-
 258 ation of T_5 and collision of the seamount with the backstop (8–12 cm of shortening in
 259 Figure 7). Just prior to the collision (12–18 cm of shortening), both the upper and lower
 260 layers of glass beads were sliding and the sand layer between two layers of glass beads
 261 underplated and was injected into T_5 . The décollement stepped up from the lower layer
 262 of glass beads to T_5 when the seamount passed. In addition, following the collision the
 263 seamount raised the backstop and opened a subduction channel beneath it (>20 cm of
 264 shortening in Figure 7). The subsequent forethrusts, T_6 and T_7 , were rooted in a décollement
 265 in the upper layer of glass beads. Finally, the toe of the backstop subsided slightly, caus-
 266 ing the lower layer of glass beads to act as a décollement.

267 Sediment outflux gradually decreased (blue line in Figure 5f), as it did during Exp. A,
268 until the seamount reached the backstop. After the seamount raised the backstop, at around
269 17–20 cm of shortening (Figure 7), sediment outflux fully recovered and even exceeded
270 its initial rate (Figure 5d). Outflux soon decreased again as the seamount subducted far-
271 ther landward and the backstop subsided (Figure 5f). The output-to-input ratio of the
272 experiment was 0.46 (Table 1).

273 4 Discussion

274 4.1 Décollement step-down and underplating

275 The gradual decrease of the outflux in Exp. A (Figure 5e) increased the influx to
276 the accretionary wedge, which increased its growth rate. During the time the upper layer
277 of glass beads acted as a décollement, the sediment above it was accreted to the wedge
278 front. As the slip switched to the lower layer of glass beads, the sediment between the
279 two layers of glass beads underplated the wedge, and frontal accretion continued. Sim-
280 ilar results have been reported in previous analogue experiments; i.e., underplating be-
281 comes significant when the outflux from the subduction channel (sediment subduction)
282 is smaller than the influx (Kukowski et al., 1994; Albert et al., 2018). The results of our
283 experiment support the conclusion that a narrowing of the subduction channel and a de-
284 crease in outflux can lead to sediment underplating the wedge and faster wedge growth.

285 If we assume that sand above the upper layer of glass beads is terrigenous sediment,
286 and that sand below this layer is hemipelagic–pelagic sediment, the former can be scraped
287 off at the wedge front and the latter may be underplated below the wedge (see Figure 8).
288 This occurs because terrigenous and hemipelagic sediments tend to be detached as a re-
289 sult of variations in diagenetic alteration (J. C. Moore, 1975) or smectite content (Vrolijk,
290 1990; Deng & Underwood, 2001), or existence of weak smectitic pelagic clay (J. C. Moore
291 et al., 2015). This can be observed in the Nankai Trough, where there is a step-down in
292 the décollement at 1–3 km depth, in the transitional region between the aseismic and
293 seismic zones (cf. Park et al., 2002; G. Kimura et al., 2007), which could be due to the
294 different physical properties of these rock types.

295 The stepping down of the décollement in this study was associated with subsidence
296 of the backstop, which was probably linked to increased overburden stress caused by thick-
297 ening of the wedge. Increased overburden stress may inhibit the subduction of terrige-

298 nous sediment to great depth. Underplating related to subsidence of the backstop (in-
 299 ner wedge) also occurs along erosive margins. For example, thick (> 2 km) sediment cover
 300 suggests subsidence of the inner wedge of the Ecuador–Colombia margin (Collot et al.,
 301 2008). Seismic profiles indicate underplating between listric splay faults and the basal
 302 décollement beneath the apex of the inner wedge, but the total mass flux at the plate
 303 interface is negative (Collot et al., 2008), and material at the base of the inner wedge
 304 is eroded.

305 4.2 Décollement step-up and sediment subduction

306 In Exp. B, the subduction of a seamount shifted the décollement from the glass bead
 307 layers into forethrust T_5 along the leading flank of the seamount. While T_5 was active
 308 as a “top décollement” (cf. Lallemand et al., 1994), incoming undeformed layered sand
 309 in the wake of the seamount was underthrust below the accretionary wedge. This is sim-
 310 ilar to what is seen in seismic profiles from the Nankai (Bangs et al., 2006) and Hiku-
 311 rangi margins (Bell et al., 2010), which show a décollement with a step-up caused by seamount
 312 subduction.

313 Another effect of seamount subduction in Exp. B is that raising the backstop widened
 314 the subduction channel, allowing thick layers of sand to subduct below the backstop through
 315 the subduction channel. In nature, if an oceanic plate with sufficiently large topographic
 316 highs subducts under a static backstop (cf. Tsuji et al., 2015), trench-fill terrigenous sed-
 317 iment accompanying the highs could be transported through the subduction channel to
 318 a higher-pressure environment than sediment on a smooth oceanic plate. Exp. B could
 319 be analogous to the transport mechanism of the protolith of the ancient Sanbagawa Meta-
 320 morphic and Shimanto Accretionary complexes of southwestern Japan.

321 We propose a schematic model for the subduction of terrigenous sediment under
 322 an accretionary wedge (Figure 8). A progressive thickening of the wedge increases the
 323 overburden on the décollement that develops along weak layers in the cover sediment de-
 324 posited on the subducting oceanic plate. This overburden results in dewatering and di-
 325 agenetic alteration of the subducting sediment, which increases its mechanical strength,
 326 leading to a step-down in the décollement (Figure 8a, b). The reduction of sediment out-
 327 flux due to narrowing of the subduction channel increases the mass of sediment under-
 328 plated beneath the wedge and the rate of frontal accretion. When a topographic high

329 (e.g., a seamount or an aseismic ridge) subducts under the wedge, the décollement steps
330 up to the forethrust along the leading flank of the seamount (Figure 8b). This likely en-
331 ables the subduction of terrigenous sediment beneath the wedge. Further subduction of
332 the topographic high would raise the backstop and open the subduction channel for ter-
333 rigenous sediment to be subducted into a high-pressure environment (Figure 8c). After
334 the topographic high passes the inner wedge or backstop, the décollement under the ac-
335 cretionary wedge returns to the plate boundary or a weak layer within the trench-fill sed-
336 iments.

337 **4.3 Further implications**

338 Excess pore pressure is important in maintaining subduction channels along the
339 plate interface (e.g., Saffer & Bekins, 2006). If the excess pore pressure drops below the
340 overburden pressure, the physical conditions in the subduction channel may resemble those
341 in the accretionary wedge (cf. Nankai and Barbados; Saffer, 2003). This probably ac-
342 celerates both the stepping down of the décollement and underplating (Strasser et al.,
343 2009; G. Kimura et al., 2011). In contrast, numerical simulations predict that the rais-
344 ing of the wedge due to the subduction of a seamount could delay the release of fluid from
345 subducting sediment (Baba et al., 2001; Ruh et al., 2016). Low-velocity layers observed
346 in the wake of subducting seamounts could provide evidence of under-compacted sed-
347 iment with potentially high excess pore pressures (e.g., Sage et al., 2006). Furthermore,
348 the seismic reflection characteristics of the Hikurangi subduction margin also suggest lo-
349 calized reductions in effective stress associated with seamount subduction (Bell et al.,
350 2010). In addition to topographic relief, excess pore pressure could allow subduction chan-
351 nels to persist for longer than would otherwise be possible. Our experiments cannot cur-
352 rently incorporate the effects of excess pore pressure; consequently, we need to consider
353 ways to include these effects.

354 Where the trench-fill sediments are insufficient to fully cover the topographic re-
355 lief of the subducting oceanic crust, tectonic erosion may dominate and the accretionary
356 wedge cannot grow, as seen in northeastern Japan, Costa Rica, and Ecuador (von Huene
357 et al., 2004; Collot et al., 2011). Therefore, a sediment-rich subduction zone is required
358 for terrigenous sediments to be transported from shallow depths (e.g., the Shimanto ac-
359 cretionary complex) to the depth of HP metamorphism (e.g., the Sanbagawa metamor-
360 phic complex).

5 Conclusions

We conducted a series of analogue experiments to investigate how terrigenous sediment is subducted under an accretionary wedge. The results yielded the following conclusions.

1. An increase in overburden stress due to progressive thickening of the accretionary wedge leads the décollement to step down and narrows the subduction channel. This accelerates the growth of the wedge through underplating and frontal accretion.
2. When a topographic high subducts under the wedge, the décollement steps up from a weak detachment layer within the incoming sediment to the forethrust along the landward flank of the seamount. This enables terrigenous sediment in the wake of the seamount to be underthrust beneath the wedge.
3. If a topographic high is rigid enough to uplift the backstop, it can widen the subduction channel to transport the terrigenous sediment that follows toward deeper environments.
4. A sufficient sediment supply to the trench and a rough oceanic crust surface are necessary for simultaneous shallow accretion, underplating of the wedge, and transportation of sediment to deeper settings as the protolith of HP–LT metamorphic rocks.

Acknowledgments

We are grateful to Takato Takemura for useful suggestions regarding experimental material and Yujiro Ogawa for discussions about sediment subduction and accretion. This work was funded by a Grant-in-Aid from the Japan Society for the Promotion of Science (17K05687). This research was supported by the Cooperative Program (No. 143, 2017; No. 147, 2018; No. 151, 2019) of the Atmosphere and Ocean Research Institute, The University of Tokyo. Relevant multimedia data files for this study are available on Figshare (<http://doi.org/10.6084/m9.figshare.10263674>).

References

Albert, F., Kukowski, N., Tassara, A., & Oncken, O. (2018). Material transfer and subduction channel segmentation at erosive continental margins: In-

- 391 sights from scaled analogue experiments. *Tectonophysics*, *749*, 46–61. doi:
392 10.1016/j.tecto.2018.10.019
- 393 Angiboust, S., Cambeses, A., Hyppolito, T., Glodny, J., Monié, P., Calderón, M.,
394 & Juliani, C. (2018). A 100-m.y.-long window onto mass-flow processes
395 in the Patagonian Mesozoic subduction zone (Diego de Almagro Island,
396 Chile). *Geological Society of America Bulletin*, *130*(9–10), 1439–1456. doi:
397 10.1130/B31891.1
- 398 Aoki, K., Iizuka, T., Hirata, T., Maruyama, S., & Terabayashi, M. (2007). Tec-
399 tonic boundary between the sanbagawa belt and the shimanto belt in central
400 shikoku, japan. *Journal of the Geological Society of Japan*, *113*(5), 171–183.
401 doi: 10.5575/geosoc.113.171
- 402 Aoki, K., Isozaki, Y., Yamamoto, S., Maki, K., Yokoyama, T., & Hirata, T. (2012).
403 Tectonic erosion in a Pacific-type orogen: Detrital zircon response to Creta-
404 ceous tectonics in Japan. *Geology*, *40*(12), 1087–1090. doi: 10.1130/G33414.1
- 405 Baba, T., Hori, T., Hirano, S., Cummins, P. R., Park, J.-O., Kameyama, M., &
406 Kaneda, Y. (2001). Deformation of a seamount subducting beneath an accre-
407 tionary prism: Constraints from numerical simulation. *Geophysical Research*
408 *Letters*, *28*(9), 1827–1830. doi: 10.1029/2000GL012266
- 409 Bangs, N. L. B., Gulick, S. P. S., & Shipley, T. H. (2006). Seamount subduction
410 erosion in the Nankai Trough and its potential impact on the seismogenic zone.
411 *Geology*, *34*(8), 701–704. doi: 10.1130/G22451.1
- 412 Barker, D. H. N., Sutherland, R., Henrys, S., & Bannister, S. (2009). Geom-
413 etry of the Hikurangi subduction thrust and upper plate, North Island,
414 New Zealand. *Geochemistry, Geophysics, Geosystems*, *10*(Q02007). doi:
415 10.1029/2008GC002153
- 416 Bell, R., Sutherland, R., Barker, D. H. N., Henrys, S., Bannister, S., Wallace,
417 L., & Beavan, J. (2010). Seismic reflection character of the Hikurangi
418 subduction interface, New Zealand, in the region of repeated Gisborne
419 slow slip events. *Geophysical Journal International*, *180*(1), 34–48. doi:
420 10.1111/j.1365-246X.2009.04401.x
- 421 Booth-Rea, G., Klaeschen, D., Grevemeyer, I., & Reston, T. (2008). Heteroge-
422 neous deformation in the Cascadia convergent margin and its relation to
423 thermal gradient (Washington, NW USA). *Tectonics*, *27*(TC4005). doi:

424 10.1029/2007TC002209

425 Buiter, S. J. H. (2012). A review of brittle compressional wedge models. *Tectono-*
 426 *physics*, 530–531, 1–17. doi: 10.1016/j.tecto.2011.12.018

427 Calvert, A. J., Preston, L. A., & Farahbod, A. M. (2011). Sedimentary underplating
 428 at the Cascadia mantle-wedge corner revealed by seismic imaging. *Nature Geo-*
 429 *science*, 4(8), 545–548. doi: 10.1038/ngeo1195

430 Collot, J. Y., Agudelo, W., Ribodetti, A., & Marcaillou, B. (2008). Origin of a
 431 crustal splay fault and its relation to the seismogenic zone and underplating
 432 at the erosional north Ecuador–south Colombia oceanic margin. *Journal of*
 433 *Geophysical Research*, 113(B12102). doi: 10.1029/2008JB005691

434 Collot, J. Y., Ribodetti, A., Agudelo, W., & Sage, F. (2011). The South Ecuador
 435 subduction channel: Evidence for a dynamic mega-shear zone from 2D fine-
 436 scale seismic reflection imaging and implications for material transfer. *Journal*
 437 *of Geophysical Research*, 116(B11). doi: 10.1029/2011JB008429

438 Dahlen, F. A. (1984). Noncohesive critical coulomb wedges: An exact so-
 439 lution. *Journal of Geophysical Research*, 89(B12), 10125–10133. doi:
 440 10.1029/JB089iB12p10125

441 Deng, X., & Underwood, M. B. (2001). Abundance of smectite and the location
 442 of a plate-boundary fault, Barbados accretionary prism. *Geological Society of*
 443 *America Bulletin*, 113(4), 495–507. doi: 10.1130/0016-7606(2001)113<\$0495:
 444 AOSATL>\$2.0.CO;2

445 Dominguez, S., Malavieille, J., & Lallemand, S. E. (2000). Deformation of accre-
 446 tionary wedges in response to seamount subduction: Insights from sandbox
 447 experiments. *Tectonics*, 19(1), 182–196. doi: 10.1029/1999TC900055

448 Dotare, T., Yamada, Y., Adam, J., Hori, T., & Sakaguchi, H. (2016). Initiation of
 449 a thrust fault revealed by analog experiments. *Tectonophysics*, 684, 148–156.
 450 doi: 10.1016/j.tecto.2015.12.023

451 Dumitru, T. A., Ernst, W. G., Hourigan, J. K., & McLaughlin, R. J. (2015). De-
 452 trital zircon U–Pb reconnaissance of the Franciscan subduction complex in
 453 northwestern California. *International Geology Review*, 57(5–8), 767–800. doi:
 454 10.1080/00206814.2015.1008060

455 Ernst, W. G. (2011). Accretion of the Franciscan Complex attending Jurassic–
 456 Cretaceous geotectonic development of northern and central California. *Geolog-*

- 457 *ical Society of America Bulletin*, 123(9–10), 1667–1678. doi: 10.1130/B30398
 458 .1
- 459 Geological Survey of Japan, AIST (Ed.). (2015). *Seamless digital geological map of*
 460 *japan 1:200,000, may 29, 2015 version*. Geological Survey of Japan, National
 461 Institute of Advanced Industrial Science and Technology. ([Cited 29 May
 462 2016]. Available from: <https://gbank.gsj.jp/seamless/index.en.html>)
- 463 Ghisetti, F. C., Barnes, P. M., Ellis, S., Plaza-Faverola, A. A., & Barker, D. H. N.
 464 (2016). The last 2 Myr of accretionary wedge construction in the central
 465 Hikurangi margin (North Island, New Zealand): Insights from structural
 466 modeling. *Geochemistry, Geophysics, Geosystems*, 17, 2661–2686. doi:
 467 10.1002/2016GC006341
- 468 Glodny, J., Lohrmann, J., Echtler, H., Gräfe, K., Seifert, W., Collao, S., & Figueroa,
 469 O. (2005). Internal dynamics of a paleoaccretionary wedge: insights from com-
 470 bined isotope tectonochronology and sandbox modelling of the South-Central
 471 Chilean forearc. *Earth and Planetary Science Letters*, 231(1), 23–39. doi:
 472 10.1016/j.epsl.2004.12.014
- 473 Graveleau, F., Malavielle, J., & Dominguez, S. (2012). Experimental modelling of
 474 orogenic wedges: A review. *Tectonophysics*, 538–540, 1–66. doi: 10.1016/j
 475 .tecto.2012.01.027
- 476 Gulick, S. P. S., Meltzer, A. M., & Clarke, S. H. (1998). Seismic structure of the
 477 southern cascadia subduction zone and accretionary prism north of the mendo-
 478 cino triple junction. *Journal of Geophysical Research*, 103(B11), 27207–27222.
 479 doi: 10.1029/98JB02526
- 480 Hara, H., & Hara, K. (2019). Radiolarian and U–Pb zircon dating of Late
 481 Cretaceous and Paleogene Shimanto accretionary complexes, Southwest
 482 Japan: Temporal variations in provenance and offset across an out-of-
 483 sequence thrust. *Journal of Asian Earth Sciences*, 170, 29–44. doi:
 484 10.1016/j.jseaes.2018.10.016
- 485 Hara, H., Nakamura, Y., Hara, K., Kurihara, T., Mori, H., Iwano, H., . . . Hirata,
 486 T. (2017). Detrital zircon multi-chronology, provenance, and low-grade meta-
 487 morphism of the Cretaceous Shimanto accretionary complex, eastern Shikoku,
 488 Southwest Japan: Tectonic evolution in response to igneous activity within a
 489 subduction zone. *Island Arc*, ??, ?? doi: 10.1111/iar.12218

- 490 Hubbert, M. K. (1937). Theory of scale models as applied to the study of geologic
491 structures. *Geological Society of America Bulletin*, 48(10), 1459–1519. doi: 10
492 .1130/GSAB-48-1459
- 493 Huot, G., & Singh, S. C. (2018). Seismic evidence for fluid/gas beneath the
494 Mentawai Fore-Arc Basin, central Sumatra. *Journal of Geophysical Research:*
495 *Solid Earth*, 123(2), 957–976. doi: 10.1002/2017JB014849
- 496 Jacobson, C. E., Grove, M., Pedrick, J. N., Barth, A. P., Marsaglia, K. M., Gehrels,
497 G. E., & Nourse, J. A. (2011). Late Cretaceous–early Cenozoic tectonic evolu-
498 tion of the southern California margin inferred from provenance of trench and
499 forearc sediments. *Geological Society of America Bulletin*, 123(3–4), 485–506.
500 doi: 10.1130/B30238.1
- 501 Jordan, T. H., Menard, H. W., & Smith, D. K. (1983). Density and size distri-
502 bution of seamounts in the eastern Pacific inferred from wide-beam sound-
503 ing data. *Journal of Geophysical Research*, 88(B12), 10508–10518. doi:
504 10.1029/JB088iB12p10508
- 505 Kiminami, K., Hamasaki, A., & Matsuura, T. (1999). Geochemical contrast between
506 the Sanbagawa psammitic schists (Oboke unit) and the Cretaceous Shimanto
507 sandstones in Shikoku, Southwest Japan and its geologic significance. *Island*
508 *Arc*, 8(3), 373–382. doi: 10.1046/j.1440-1738.1999.00248.x
- 509 Kimura, G., Kitamura, Y., Hashimoto, Y., Yamaguchi, A., Shibata, T., Ujiie, K., &
510 Okamoto, S. (2007). Transition of accretionary wedge structures around the
511 up-dip limit of the seismogenic subduction zone. *Earth and Planetary Science*
512 *Letters*, 255(3–4), 471–484. doi: 10.1016/j.epsl.2007.01.005
- 513 Kimura, G., Moore, G. F., Strasser, M., Sreaton, E., Curewitz, D., Streiff, C., &
514 Tobin, H. (2011). Spatial and temporal evolution of the megasplay fault in
515 the Nankai Trough. *Geochemistry, Geophysics, Geosystems*, 12(Q0A008). doi:
516 10.1029/2010GC003335
- 517 Kimura, H., Takeda, T., Obara, K., & Kasahara, K. (2010). Seismic evidence for
518 active underplating below the megathrust earthquake zone in Japan. *Science*,
519 329(5988), 210–212. doi: 10.1126/science.1187115
- 520 Kopp, H., Hindle, D., Klaeschen, D., Oncken, O., Reichert, C., & Scholl, D. (2009).
521 Anatomy of the western Java plate interface from depth-migrated seismic
522 images. *Earth and Planetary Science Letters*, 288(3–4), 399–407. doi:

- 523 10.1016/j.epsl.2009.09.043
- 524 Kukowski, N., von Huene, R., Malavieille, J., & Lallemand, S. E. (1994). Sediment
525 accretion against a buttress beneath the Peruvian continental margin at 12° S
526 as simulated with sandbox modeling. *Geologische Rundschau*, 83(4), 822–831.
527 doi: 10.1007/BF00251079
- 528 Lallemand, S. E., Malavieille, J., & Calassou, S. (1992). Effects of oceanic ridge
529 subduction on accretionary wedges; experimental modeling and marine obser-
530 vations. *Tectonics*, 11(6), 1301–1313. doi: 10.1029/92TC00637
- 531 Lallemand, S. E., Schnürle, P., & Malavieille, J. (1994). Coulomb theory applied to
532 accretionary and nonaccretionary wedges: Possible causes for tectonic erosion
533 and/or frontal accretion. *Journal of Geophysical Research*, 99(B6), 12033–
534 12055. doi: 10.1029/94JB00124
- 535 Li, J., Shillington, D. J., Saffer, D. M., Bécel, A., Nedimović, M. R., Kuehn, H., ...
536 Abers, G. A. (2018). Connections between subducted sediment, pore-fluid
537 pressure, and earthquake behavior along the Alaska megathrust. *Geology*,
538 46(4), 299–302. doi: 10.1130/G39557.1
- 539 Lohrmann, J., Kukowski, N., Adam, J., & Oncken, O. (2003). The impact of
540 analogue material properties on the geometry, kinematics, and dynamics of
541 convergent sand wedges. *Journal of Structural Geology*, 25(10), 1691–1711.
542 doi: 10.1016/S0191-8141(03)00005-1
- 543 Melnick, D., Bookhagen, B., Echtler, H. P., & Strecker, M. R. (2006). Coastal
544 deformation and great subduction earthquakes, Isla Santa María, Chile
545 (37°S). *Geological Society of America Bulletin*, 118(11–12), 1463–1480. doi:
546 10.1130/B25865.1
- 547 Milliman, J. D., & Syvitski, J. P. M. (1992). Geomorphic/tectonic control of sed-
548 iment discharge to the ocean: The importance of small mountainous rivers.
549 *Journal of Geology*, 100(5), 525–544. doi: 10.1086/629606
- 550 Moore, G. F., Kanagawa, K., Strasser, M., Dugan, B., Maeda, L., Toczko, S., & the
551 IODP Expedition 338 Scientific Party. (2014). IODP Expedition 338: NanTro-
552 SEIZE Stage 3: NanTroSEIZE plate boundary deep riser 2. *Scientific Drilling*,
553 17, 1–12. doi: 10.5194/sd-17-1-2014
- 554 Moore, G. F., Taira, A., Klaus, A., Becker, L., Boeckel, B., Cragg, B. A., ...
555 Wilson, M. (2001). New insights into deformation and fluid flow pro-

- 556 cesses in the Nankai Trough accretionary prism: Results of Ocean Drilling
 557 Program Leg 190. *Geochemistry, Geophysics, Geosystems*, 2(1058). doi:
 558 10.1029/2001GC000166
- 559 Moore, G. F., Zhao, Z., Shipley, T. H., Bangs, N., & Moore, J. C. (1995). Structural
 560 setting of the Leg 156 area, northern Barbados Ridge accretionary prism. In
 561 T. H. Shipley, Y. Ogawa, P. Blum, & et al. (Eds.), *Proceedings of the Ocean*
 562 *Drilling Program, Initial Reports* (Vol. 156, pp. 13–27). College Station, TX:
 563 Ocean Drilling Program. doi: 10.2973/odp.proc.ir.156.102.1995
- 564 Moore, J. C. (1975). Selective subduction. *Geology*, 3(9), 530–532. doi: 10.1130/
 565 0091-7613(1975)3:530:SS;2-0.CO;2
- 566 Moore, J. C., Diebold, J., Fisher, M. A., Sample, J., Brocher, T., Talwani, M.,
 567 ... Sawyer, D. (1991). Edge deep seismic reflection transect of the eastern
 568 Aleutian arc-trench layered lower crust reveals underplating and continental
 569 growth. *Geology*, 19(5), 420–424. doi: 10.1130/0091-7613(1991)019:420:
 570 EDSRTO;2-3.CO;2
- 571 Moore, J. C., Plank, T. A., Chester, F. M., Polissar, P. J., & Savage, H. M. (2015).
 572 Sediment provenance and controls on slip propagation: Lessons learned from
 573 the 2011 Tohoku and other great earthquakes of the subducting northwest
 574 Pacific plate. *Geosphere*, 11(3), 533–541. doi: 10.1130/GES01099.1
- 575 Morgan, J. K., & Bangs, N. L. (2017). Recognizing seamount-forearc collisions at
 576 accretionary margins: Insights from discrete numerical simulations. *Geology*,
 577 45(7), 635–638. doi: 10.1130/G38923.1
- 578 Nagata, M., Miyazaki, K., Iwano, H., Danhara, T., Obayashi, H., Hirata, T., ...
 579 Otoh, S. (2019). Timescale of material circulation in subduction zone: U–Pb
 580 zircon and K–Ar phengite double-dating of the Sanbagawa metamorphic com-
 581 plex in the Ikeda district, central Shikoku, southwest Japan. *Island Arc*, 28(4),
 582 e12306. doi: 10.1111/iar.12306
- 583 Noda, A. (2016). Forearc basins: Types, geometries, and relationships to subduction
 584 zone dynamics. *Geological Society of America Bulletin*, 128(5–6), 879–895. doi:
 585 10.1130/B31345.1
- 586 Noda, A., Danhara, T., Iwano, H., & Hirata, T. (2017). LA-ICP-MS U–Pb and
 587 fission-track ages of felsic tuff beds of the Takikubo Formation, Izumi Group
 588 in the Kan-onji district, eastern Shikoku, southwestern Japan. *Bulletin of the*

- 589 *Geological Survey of Japan*, 68(3), 119–130. doi: 10.9795/bullgsj.68.119
- 590 Noda, A., Danhara, T., Iwano, H., & Hirata, T. (accepted). LA-ICP-MS zircon
591 U–Pb ages of felsic tuffaceous beds in the Takikubo and Horita formations,
592 Izumi Group, Ikeda district, eastern Shikoku, southwestern Japan. *Bulletin of*
593 *the Geological Survey of Japan*.
- 594 Noda, A., & Sato, D. (2018). Submarine slope–fan sedimentation in an an-
595 cient forearc related to contemporaneous magmatism: The Upper Creta-
596 ceous Izumi Group, southwestern Japan. *Island Arc*, 27(2), e12240. doi:
597 10.1111/iar.12240
- 598 Okay, A. I., Tüysüz, O., Satır, M., özkan Altiner, S., Altiner, D., Sherlock, S., &
599 Eren, R. H. (2006). Cretaceous and Triassic subduction-accretion, high-
600 pressure–low-temperature metamorphism, and continental growth in the Cen-
601 tral Pontides, Turkey. *Geological Society of America Bulletin*, 118(9–10),
602 1247–1269. doi: 10.1130/B25938.1
- 603 Otoh, S., Shimojo, M., Aoki, K., Nakama, T., Maruyama, S., & Yanai, S. (2010).
604 Age distribution of detrital zircons in the psammitic schist of the Sanbagawa
605 Belt, Southwest Japan. *Journal of Geography (Chigaku Zasshi)*, 119(2), 333–
606 346. doi: 10.5026/jgeography.119.333
- 607 Park, J.-O., Tsuru, T., Takahashi, N., Hori, T., Kodaira, S., Nakanishi, A., ...
608 Kaneda, Y. (2002). A deep strong reflector in the Nankai accretionary wedge
609 from multichannel seismic data: Implications for underplating and interseis-
610 mic shear stress release. *Journal of Geophysical Research*, 107(B4). doi:
611 10.1029/2001JB000262
- 612 Plafker, G., Moore, J. C., & Winkler, G. R. (1994). Geology of the southern alaska
613 margin. In G. Plafker & H. C. Berg (Eds.), *The geology of alaska* (Vols. G–1,
614 pp. 389–449). Boulder, Colorado, United States: Geological Society of Amer-
615 ica. doi: 10.1130/DNAG-GNA-G1.389
- 616 Plaza-Faverola, A., Henrys, S., Pecher, I., Wallace, L., & Klaeschen, D. (2016).
617 Splay fault branching from the Hikurangi subduction shear zone: Implica-
618 tions for slow slip and fluid flow. *Geochemistry, Geophysics, Geosystems*, 17,
619 5009–5023. doi: 10.1002/2016GC006563
- 620 Raymond, L. A. (2018). What is Franciscan?: revisited. *International Geology Re-*
621 *view*, 60(16), 1968–2030. doi: 10.1080/00206814.2017.1396933

- 622 Ruh, J. B., Sallarès, V., Ranero, C. R., & Gerya, T. (2016). Crustal deformation
 623 dynamics and stress evolution during seamount subduction: High-resolution
 624 3-D numerical modeling. *Journal of Geophysical Research: Solid Earth*, *121*,
 625 6880–6902. doi: 10.1002/2016JB013250
- 626 Saffer, D. M. (2003). Pore pressure development and progressive dewatering in un-
 627 derthrust sediments at the Costa Rican subduction margin: Comparison with
 628 northern Barbados and Nankai. *Journal of Geophysical Research*, *108*(B5,
 629 2261). doi: 10.1029/2002JB001787
- 630 Saffer, D. M., & Bekins, B. A. (2006). An evaluation of factors influencing
 631 pore pressure in accretionary complexes; implications for taper angle and
 632 wedge mechanics. *Journal of Geophysical Research*, *111*(B04101). doi:
 633 10.1029/2005JB003990
- 634 Sage, F., Collot, J. Y., & Ranero, C. R. (2006). Interplate patchiness and
 635 subduction-erosion mechanisms: Evidence from depth-migrated seismic im-
 636 ages at the central Ecuador convergent margin. *Geology*, *34*(12), 997–1000.
 637 doi: 10.1130/G22790A.1
- 638 Sample, J. C., & Moore, J. C. (1987). Structural style and kinematics of an un-
 639 derplated slate belt, Kodiak and adjacent islands, Alaska. *Geological Soci-
 640 ety of America Bulletin*, *99*(1), 7–20. doi: 10.1130/0016-7606(1987)99\$;7:
 641 SSAKOA\$;2.0.CO;2
- 642 Schellart, W. P. (2000). Shear test results for cohesion and friction coeffi-
 643 cients for different granular materials: scaling implications for their usage
 644 in analogue modelling. *Tectonophysics*, *324*(1–2), 1–16. doi: 10.1016/
 645 S0040-1951(00)00111-6
- 646 Schellart, W. P., & Strak, V. (2016). A review of analogue modelling of geodynamic
 647 processes: Approaches, scaling, materials and quantification, with an appli-
 648 cation to subduction experiments. *Journal of Geodynamics*, *100*, 7–32. doi:
 649 10.1016/j.jog.2016.03.009
- 650 Scholl, D. W. (2019). Seismic imaging evidence that forearc underplating built the
 651 accretionary rock record of coastal North and South America. *Geological Mag-
 652 azine*, *??*, 1–14. doi: 10.1017/S0016756819000955
- 653 Schumann, K., Behrmann, J. H., Stipp, M., Yamamoto, Y., Kitamura, Y., & Lempp,
 654 C. (2014). Geotechnical behavior of mudstones from the Shimanto and Boso

- 655 accretionary complexes, and implications for the Nankai accretionary prism.
 656 *Earth, Planets and Space*, *66*(1), 129. doi: 10.1186/1880-5981-66-129
- 657 Shibata, T., Orihashi, Y., Kimura, G., & Hashimoto, Y. (2008). Underplating of
 658 mélangé evidenced by the depositional ages: U–Pb dating of zircons from the
 659 Shimanto accretionary complex, southwest Japan. *Island Arc*, *17*(3), 376–393.
 660 doi: 10.1111/j.1440-1738.2008.00626.x
- 661 Singh, S. C., Carton, H., Tapponnier, P., Hananto, N. D., Chauhan, A. P. S., Har-
 662 toyo, D., ... Martin, J. (2008). Seismic evidence for broken oceanic crust in
 663 the 2004 Sumatra earthquake epicentral region. *Nature Geoscience*, *1*(11),
 664 777–781. doi: 10.1038/ngeo336
- 665 Smith, D. K. (1988). Shape analysis of Pacific seamounts. *Earth and Planetary Sci-*
 666 *ence Letters*, *90*(4), 457–466. doi: 10.1016/0012-821X(88)90143-4
- 667 Strasser, M., Moore, G. F., Kimura, G., Kitamura, Y., Kopf, A. J., Lallemand, S.,
 668 ... Zhao, X. (2009). Origin and evolution of a splay fault in the Nankai ac-
 669 cretionary wedge. *Nature Geoscience*, *2*(9), 648–652. doi: 10.1038/NGEO609
- 670 Tsuji, T., Ashi, J., Strasser, M., & Kimura, G. (2015). Identification of the static
 671 backstop and its influence on the evolution of the accretionary prism in the
 672 Nankai Trough. *Earth and Planetary Science Letters*, *431*, 15–25. doi:
 673 10.1016/j.epsl.2015.09.011
- 674 Vannucchi, P., Remitti, F., & Bettelli, G. (2008). Geological record of fluid flow and
 675 seismogenesis along an erosive subducting plate boundary. *Nature*, *451*(7179),
 676 699–703. doi: 10.1038/nature06486
- 677 von Huene, R., & Culotta, R. (1989). Tectonic erosion at the front of the Japan
 678 Trench convergent margin. *Tectonophysics*, *160*, 75–90. doi: 10.1016/0040-
 679 -1951(89)90385-5
- 680 von Huene, R., Ranero, C. R., & Vannucchi, P. (2004). Generic model of subduction
 681 erosion. *Geology*, *32*(10), 913–916. doi: 10.1130/G20563.1
- 682 Vrolijk, P. (1990). On the mechanical role of smectite in subduction zones. *Geology*,
 683 *18*(8), 703–707. doi: 10.1130/0091-7613(1990)018<\$;0703:OTMROS\$;2.3.CO;
 684 2
- 685 Wallis, S. (1998). Exhuming the Sanbagawa metamorphic belt: the importance of
 686 tectonic discontinuities. *Journal of Metamorphic Geology*, *16*(1), 83–95. doi:
 687 10.1111/j.1525-1314.1998.00072.x

688 Willner, A. P., Glodny, J., Gerya, T. V., Godoy, E., & Massonne, H. J. (2004). A
689 counterclockwise PTt path of high-pressure/low-temperature rocks from the
690 Coastal Cordillera accretionary complex of south-central Chile: constraints
691 for the earliest stage of subduction mass flow. *Lithos*, *75*(3), 283–310. doi:
692 10.1016/j.lithos.2004.03.002

693 Yamada, Y., Baba, K., Miyakawa, A., & Matsuoka, T. (2014). Granular experi-
694 ments of thrust wedges: Insights relevant to methane hydrate exploration at
695 the Nankai accretionary prism. *Marine and Petroleum Geology*, *51*, 34–48. doi:
696 10.1016/j.marpetgeo.2013.11.008

697 Yamada, Y., Kaneda, K., & Matsuoka, T. (2006). Influences of material properties
698 on analogue model experiments of geologic structures. *Journal of the Society of*
699 *Materials Science, Japan*, *55*(5), 452–457. (in Japanese with English abstract)
700 doi: 10.2472/jsms.55.452

701 Ye, S., Flueh, E. R., Klaeschen, D., & von Huene, R. (1997). Crustal structure along
702 the EDGE transect beneath the Kodiak shelf off Alaska derived from OBH
703 seismic refraction data. *Geophysical Journal International*, *130*(2), 283–302.
704 doi: 10.1111/j.1365-246X.1997.tb05648.x

Table 1. Total sediment input and output, and their ratio. Asterisk (*) indicates output includes the volume of the seamount.

Exp.	Displacement (cm)	Input (cm ³)	Output* (cm ³)	Accretion (cm ³)	Output/Input Ratio
A	30.0	2,912	1,052	1,860	0.36
B	35.0	3,315	1,527	1,788	0.46

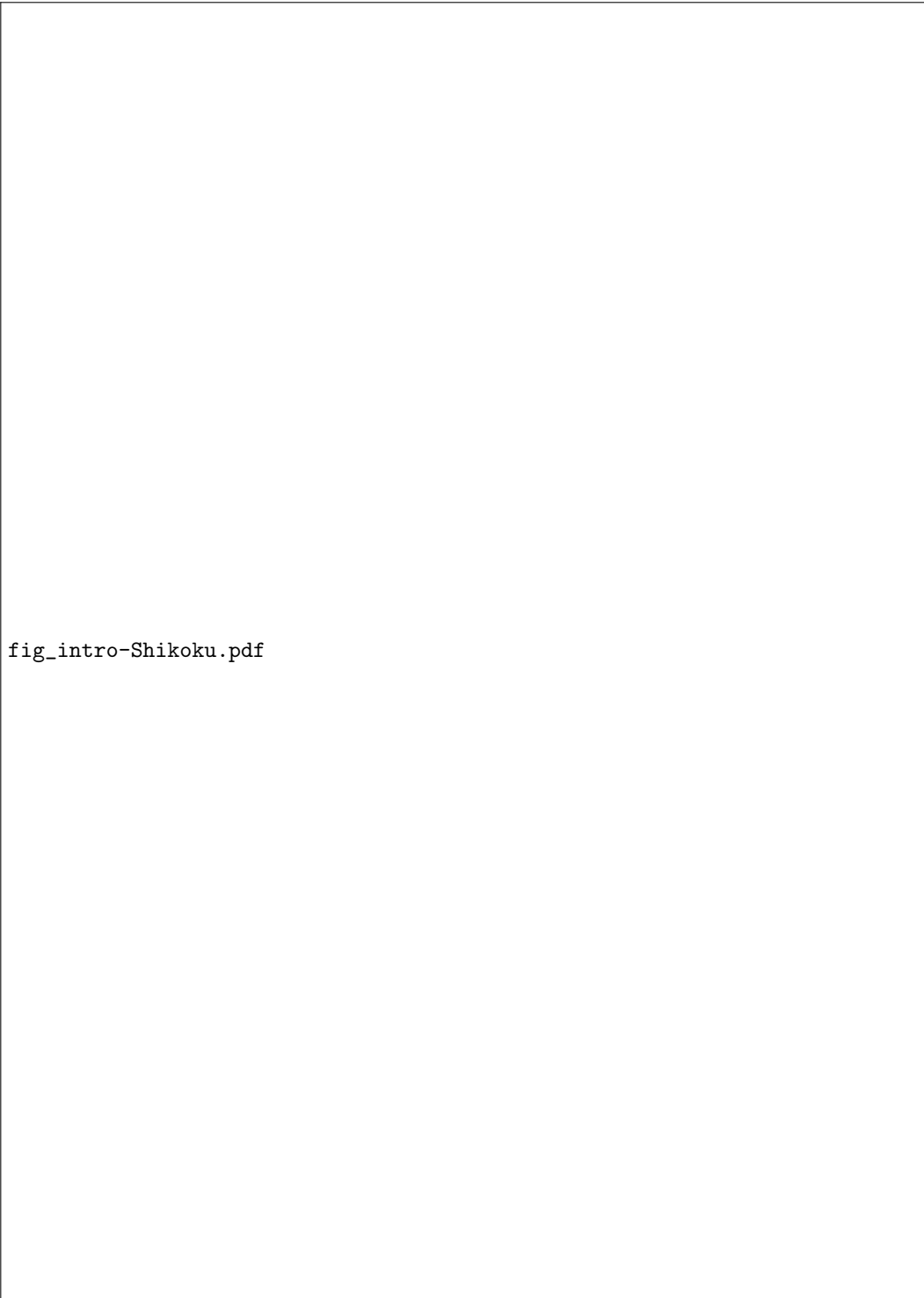


Figure 1. Generalized geological map of eastern Shikoku, southwestern Japan, reproduced from the Seamless Digital Geological Map of Japan (Geological Survey of Japan, AIST, 2015). Black dots are labeled with detrital zircon U–Pb ages (Ma) of felsic tuff beds in the Izumi Group, composed mainly of sandy turbidites and mudstone (Noda et al., 2017, accepted), the psammitic schist of the Sanbagawa Metamorphic Complex (Aoki et al., 2007; Nagata et al., 2019; Otoh et al., 2010), and sandy turbidites in the northern Shimanto Accretionary Complex (Hara et al., 2017; Hara & Hara, 2019; Shibata et al., 2008).^{–25–}

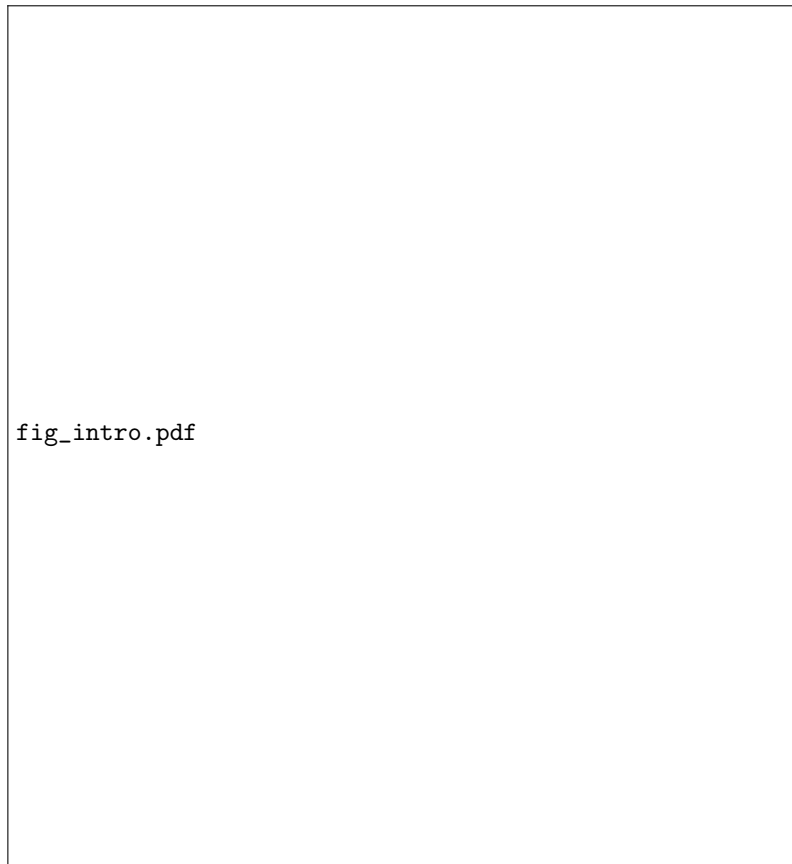


Figure 2. Representative cross-sections of accretionary margins with topographic highs. (a) Nankai Trough (G. F. Moore et al., 2014). (b) Southwestern Alaskan margin (Li et al., 2018). (c) Northern Barbados margin (G. F. Moore et al., 1995).

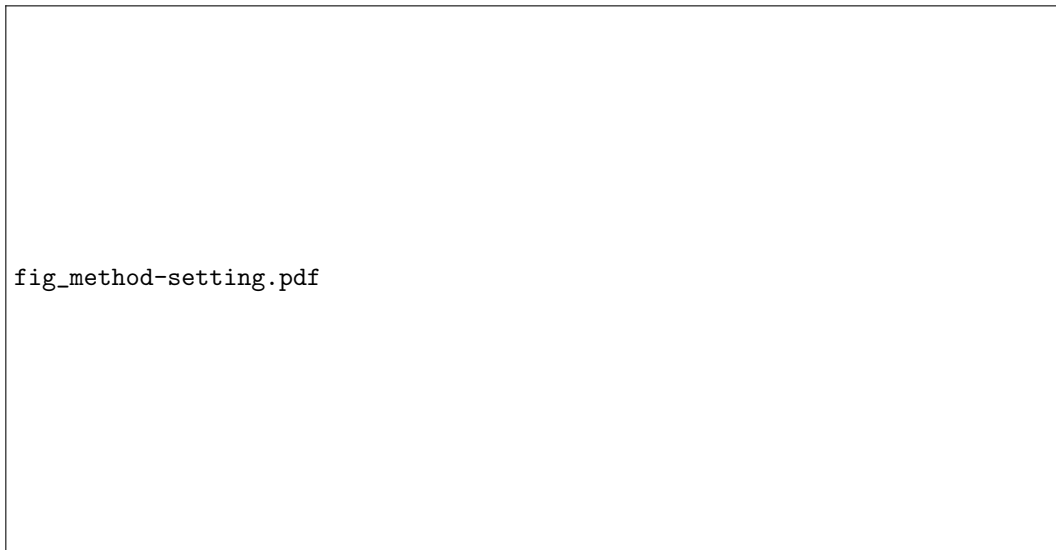


Figure 3. Experimental apparatus.



Figure 4. Amount of sand added to the topographic lows during the experiments.

fig_res-param.pdf

Figure 5. Geomorphic parameters of the wedges (a-d) and sediment fluxes (e-f). (a) Number of forethrusts. (b) Wedge width. Dashed lines are labelled with wedge progradation rates calculated from the amount of progradation (cm) divided by the amount of shortening (cm). (c) Wedge slope angle. (d) Wedge height. Dashed lines are labelled with uplift rates calculated from the amount of uplift (cm) divided by the amount of shortening (cm). (e) Sediment influx and outflux for Exp. A (without seamount). (f) Sediment influx and outflux for Exp. B (with seamount). Asterisk (*) and dagger (†) indicate outfluxes including and excluding the volume of the seamount, respectively.

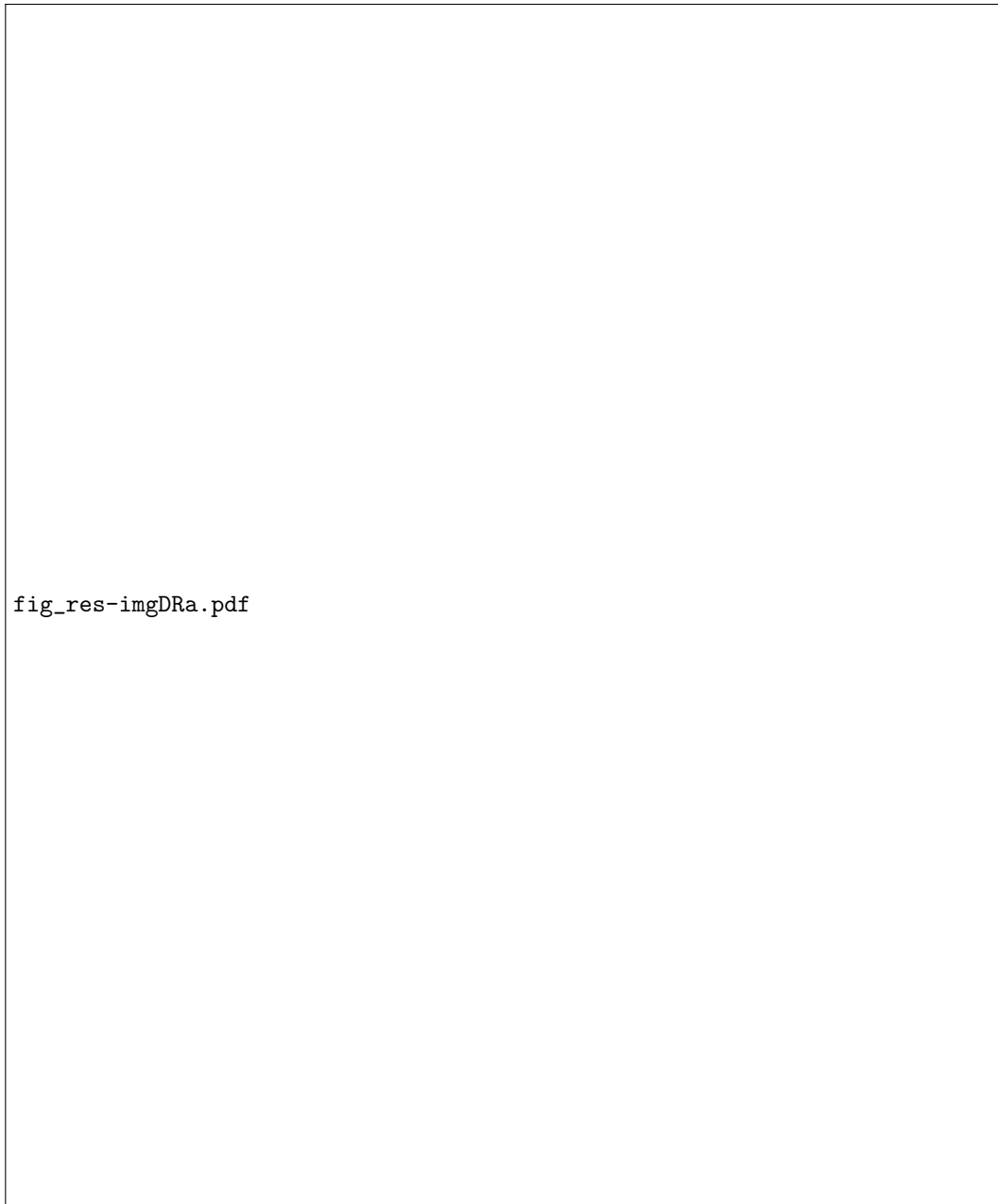
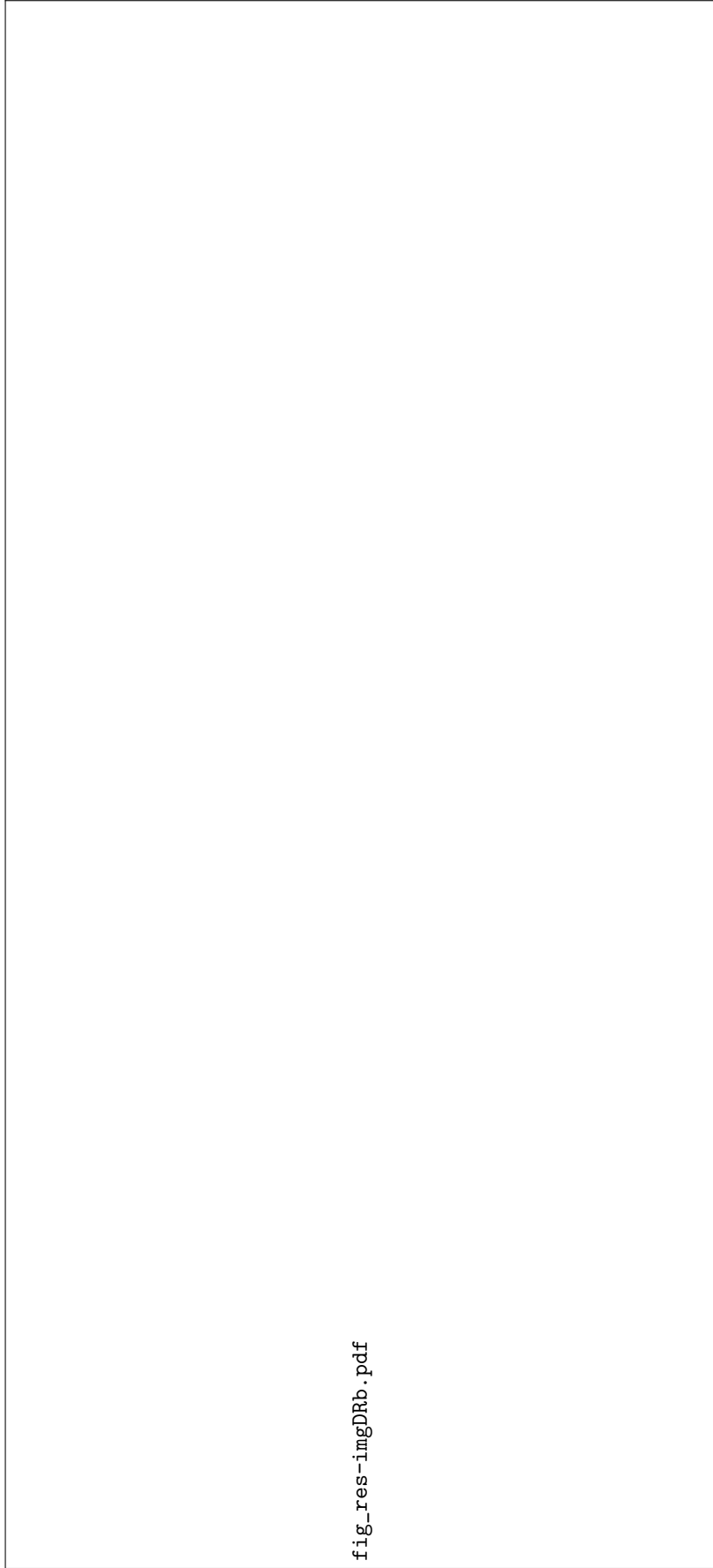


Figure 6. Representative images of Exp. A.



fig_res_imgDRb.pdf

Figure 7. Representative images of Exp. B.



Figure 8. Schematic model of sediment subduction through a subduction channel beneath an accretionary wedge. (a) Subduction of a topographic high raises the décollement to accommodate the high and the following trench-fill sediment. (b) An increase in overburden gravitational force under the inner wedge shifts the décollement downward and facilitates underplating. In the wake of the subducting seamount, terrigenous sediment is underthrust beneath the accretionary wedge. (c) The seamount raises the backstop, enabling the subduction of terrigenous sediment. After the passage of the seamount, the décollement returns to the original, lower position, and the subduction channel closes, resulting in underplating beneath the wedge.